Supplementary Information

Enabling superior high-temperature capacitive performance in polymer dielectrics by multifunctional alternating nanolaminate coating

Yuqi Liu,‡[abc] Jiufeng Dong,‡[ab] Kaixin Liu,‡[ab] Chengyuan Wang,[ab] Yujuan Niu,[ab] Liang Sun,[ab] Shuoyan Liu,[ab] Jiangyu Li,[ab] Jiannong Wang*[c] and Hong Wang*[ab]*

[a] *State Key Laboratory of Quantum Functional Materials, Department of Materials Science and Engineering, Southern University of Science and Technology, Shenzhen 518055, Guangdong, China.*

[b] *Guangdong Provincial Key Laboratory of Functional Oxide Materials and Devices & Shenzhen Engineering Research Center for Novel Electronic Information Materials and Devices, Southern University of Science and Technology, Shenzhen 518055, Guangdong, China.*

[c] *Department of Physics, The Hong Kong University of Science and Technology, Clear Water Bay, Hong Kong, China.*

Email: dongjf@mail.sustech.edu.cn, wangh6@sustech.edu.cn, phjwang@ust.hk

‡These authors contributed equally.

Experimental

Materials

The free-standing polymer films of biaxially oriented polypropylene (BOPP), Polyetherimide (PEI), polyethylene naphthalate (PEN), polyphenylene sulfide (PPS), fluorene polyester (FPE), and polycarbonate (PC) pellets were supplied by Polyk Technologies. N,N-dimethylacetamide (DMAc, ≥99.8%) were purchased from Aladdin Chemistry Co., Ltd., China. The precursors for atomic layer deposition (ALD), including trimethylaluminum ($Al(CH_3)_3$), tetrakis(dimethylamido)zirconium ($Zr(N(CH_3)_2)_4$), and tetrakis(dimethylamido)titanium ($Ti(N(CH_3)_2)_4$), were obtained from Aimouyuan Scientific Equipment Co., Ltd. (Nanjing, China). All chemicals were used directly without further treatment.

Film Preparation

Polycarbonate (PC) pellets were dissolved in DMAc and stirred overnight to yield a clear and transparent solution. The solution was drop-casted on a re-cleaned glass plate. The cast film was dried at 120 °C for 12 hours, and subsequently peeled off from the substrate in DI water followed by drying in a vacuum oven at 120 °C for another 12 hours to remove solvent residue and water. The typical thickness of PC films is 9–13 μm.

Oxide coatings were carried out using a commercial ALD system. The polymer films were positioned approximately 3 cm from the precursor inlet nozzle. During the deposition process, nitrogen (N_2) was introduced as the carrier gas at a flow rate of 1000 SCCM, and the system pressure was maintained at 1.4 Torr. All oxide films were deposited at 120 °C, with the chamber temperature consistently held at 120 °C. The precursors and corresponding ALD sequences for each type of oxide are summarized in the table below. The table lists each ALD cycle's precursor pulse and nitrogen purge times. Each ALD cycle deposited 0.1 nm of oxide, and the total thickness of the oxide layers was controlled by adjusting the number of deposition cycles.

Structural characterizations

X-ray photoelectron spectroscopy (XPS) analysis was examined using a Thermo Fisher ESCALAB Xi+ spectrometer equipped with an Al Kα source. (UPS) was carried out on a Thermo Scientific ESCALAB Xi+ with the He-I lamp radiation (21.2 eV) and the Fermi level was calibrated using clean Au. The work function was calculated based on the binding energy of secondary electron edge (E_{SEE}) (ϕ=21.2 eV-E_{SEE}). The ionization potential (IP) was calculated based on the binding energy of onset of the E_{HOMO} (IP= 21.2-(E_{SEE}-E_{HOMO})). All samples were fixed on the sample stage with conductive glue to ensure conductivity. The ultraviolet-visible (UV–vis) spectroscopy was measured using Lambda 950 spectrophotometer to obtain the bandgap. Cross-sectional transmission electron microscopy (TEM) images of the

Al_2O_3/ZrO_2 alternating nanolaminates were obtained by Talos F200X. The FIB system used was the Scios 2 model with a Ga ion source. Both AFM topography and Kelvin probe force microscopy (KPFM) surface potential measurements were characterized using scanning probe microscopy (MFP3D-Infinity, Oxford Instruments, USA) with a conductive probe (PPP-EFM tip, ~70 kHz and ~2.8 N m^{-1}). Young's modulus was derived from stress-strain curves measured using a dynamic mechanical analyzer (DMA 850, TA Instruments), with a constant linear stretching rate of 2.0 mm min^{-1}.

Dielectric properties and energy storage properties measurements

Gold electrodes, having diameters of 3 mm, 6 mm, and 10 mm, were evaporated onto both sides of the polymer films specifically for electrical measurements. For broadband dielectric spectroscopy, the system consists of a Partulab DMS-2000 temperature-controlling chamber coupled with the Keysight 4980A analyzer. The electric displacement-electric field (*D-E*) loops of the polymer films were carried out using the ferroelectric analysis system developed by PolyK technologies. This advanced platform integrates real-time measurement modules to capture discharge energy density (U_e) and charge-discharge efficiency (η). High-voltage signals were supplied by a Trek Model 20/20C bipolar power amplifier, with an output voltage range of ±20 kV. Direct-current (DC) breakdown strength measurements of the polymer films were also performed on the PolyK workstation using a constant ramp-rate voltage protocol at 500 V s^{-1}. During testing, temperature was precisely controlled using an oil-bath thermostatic system combined with a thermocouple sensor, achieving a control accuracy of ±0.1 °C. The breakdown strength results were calculated using a two-parameter Weibull statistic described as:

$$P(E) = 1 - \exp\left(-\left(\frac{E}{E_b}\right)^{\beta}\right) \quad (S1)$$

where $P(E)$ is the cumulative probability of electric failure, E is the measured breakdown field, E_b is the field strength for which there is a 63.2% probability for the sample to breakdown, and shape parameter β evaluates the scatter of data. A higher value of β represents a higher level of dielectric reliability.[S1]

Electric conduction measurements

The high-field leakage currents of the polymer films were tested using a Keysight B2985 pA electrometer and a Stanford PS365 ±10 kV high-voltage amplifier. The testing temperature was controlled using a Delta 9023 oven. TSDC was measured using Keithley 6517B electrometer with the following recipe. The samples were first polarized under 20 MV m^{-1} DC electric field at 200 ℃ for 30 min and then rapidly cooled down to -50 ℃ with the applied electric field. Afterward, the samples were placed at -50 ℃ for 10 min, and then the electric field was

removed. Finally, the samples were short-circuited and heated to 240 ℃ at the heating rate of 3 ℃ min^{-1} with the current recorded. The Pockels effect charge measurement was employed to investigate charge injection and dissipation behaviors. Specifically, a needle–plate electrode configuration was used to apply a charging current to the sample surface, with the needle electrode positioned 0.5 mm above the material and a voltage of 1000 V applied to inject surface charges. The accumulation and dissipation of charges of the material were monitored in real time *via* Pockels signal measurement system.

For KPFM test samples, gold electrodes were deposited on the nanolayer coated polymer films' top and bottom surfaces using electron beam deposition to construct the electrode structure. Subsequently, the samples were embedded in epoxy resin and processed through frozen section to obtain smooth film cross-sections for subsequent characterization of internal charge distribution. During the testing phase, a DC voltage of 5 V was applied across both ends of the cross-sectional sample and maintained for 2 h to facilitate charge injection and distribution within the material, after which the bias was removed. The sample was then allowed to discharge for 5 min to provide a pathway for subsequent charge migration and surface charges to fully dissipate. Surface potential images were finally acquired using KPFM scanning.

To evaluate charge-blocking and trapping behavior, a surface potential difference method was employed. As shown in Figure S12 to Figure S15, in-depth surface potential profiles within a selected region were extracted from the surface potential images acquired before charging and after charging/discharging. The resulting smoothed surface potential difference profiles are presented in Figure S16. The surface potential difference reflects the variation in surface potential induced by electrical charging, representing the true electrostatic potential change. This metric therefore provides direct evidence for the charge-blocking capability of the multilayer-structured composite dielectric samples.

Furthermore, the bulk charge density distributions were calculated. According to the one-dimensional second-order electrostatic Poisson equation, the spatial variation of the surface potential under static conditions reflects the charge distribution along the depth direction. The Poisson equation is given by:

$$\frac{d^2V}{dx^2} = -\frac{q\rho}{\varepsilon\varepsilon_0} \#(S2)$$

where V denotes the surface potential, x represents the spatial coordinate, ρ is the charge density, ε_0 is the vacuum permittivity (8.854×10^{-12} F m^{-1}), and ε is the relative dielectric constant of the material.

The Pockels effect-based surface charge dynamic measurement technique is an advanced characterization method utilizing the linear electro-optic effect[S2,S3]. It enables non-contact charge detection by monitoring the refractive index changes of an electro-optic crystal under an external electric field. The system adopts a reflective optical path topology and comprises two subsystems: optics and electronics. The optical subsystem includes a 632.8 nm He-Ne laser, a polarized beam splitter, a 1/8 waveplate, and a high-speed camera (Phantom V2012, 50,000 fps, 1 μs exposure time); the electrical subsystem is equipped with a high-voltage amplifier (Trek 30/20A) and a synchronized acquisition system. Based on the two-dimensional Fourier transform algorithm (2D-FTA), this method achieves a charge density detection limit of 10 nC cm^{-2} and a spatial resolution of 512 × 512 pixels, enabling in-situ observation of charge evolution over a timescale of 0.5 s. Compared with conventional electrostatic probe methods, this technique offers millisecond-level temporal resolution, full-field two-dimensional imaging, and compatibility with opaque materials. These advantages make it a powerful experimental tool for investigating surface charge transport mechanisms in polymer insulating materials. In this study, the Pockels effect-based surface charge dynamic measurement was employed to characterize the absorption and dissipation behavior of charges in the tested materials.

Phase-field simulation of electrical breakdown

The phase-field method was employed in this work to construct an evolution model for electrical breakdown, wherein an order parameter $s(r,t)$ was introduced to characterize the local damage state of the dielectric material. Specifically, $s(r,t) = 1$ represents an intact material, $s(r,t) = 0$ indicates complete breakdown, and $0<s<1$ corresponds to the transition region, representing the interface between the intact and the broken-down phases. To capture the variation of the dielectric constant with the degree of material damage, the relative permittivity was defined as a function of the order parameter as follows:

$$\varepsilon_r(s) = \frac{\varepsilon_{r0}}{f(s) + \eta} \#\ (S3)$$

where ε_{r0} denotes the dielectric constant of the undamaged material. Upon electrical breakdown, the dielectric constant increases sharply. To prevent numerical divergence, a regularization parameter $\eta=0.001$ is introduced. The function $f(s)$ is a smooth and continuous degradation function defined over the interfacial transition region, satisfying $f(0)=0$ and $f(1)=1$. Since neither the intact phase nor the fully broken-down phase should exhibit a spontaneous phase transition tendency, the conditions $f'(0)=0$ and $f'(1)=0$ are also required. In this work, the interpolation function $f(s)=4s^3-3s^4$ is adopted as the degradation function. To simulate the

evolution of the damaged region, the time evolution of the order parameter is governed by a linear gradient dynamic's equation:

$$\frac{\partial s(r,t)}{\partial t} = -L_0 \frac{\delta F(r,t)}{\delta s(r,t)} \#(S4)$$

where L_0 is the kinetic coefficient governing the interface migration, and $F(r,t)$ denotes the free energy functional of the system, which comprehensively accounts for the electrostatic energy, the separation energy associated with the breakdown phase, and the gradient energy of the order parameter:

$$F = \int_V \left[f_{\text{elec}} + f_{\text{sep}} + f_{\text{grad}(s)} \right] dV \#(S5)$$

substituting energy into the dynamic equation, we get:

$$\frac{\partial s(r,t)}{\partial t} = -L_0 \left[\frac{\dot{f}(s)}{2[f(s)+\eta]^2} \frac{\partial \phi \partial \phi}{\partial x_i \partial x_i} + 2w_c(1-s)(1-2s) - \frac{1}{2} \frac{\partial^2 s}{\partial x_i \partial x_i} \right] \#(S6)$$

where t and w_c represent time and the breakdown energy coefficient, respectively. During the evolution of electrical treeing, the distribution of electric field and potential must satisfy the Poisson equation from Maxwell's equations under electrostatic conditions:

$$\frac{\partial}{\partial x_i} \left[\varepsilon_r(s) \frac{\partial \phi}{\partial x_i} \right] = 0 \#(S7)$$

In this study, the above system of equations was solved using the Partial Differential Equations module in COMSOL Multiphysics.

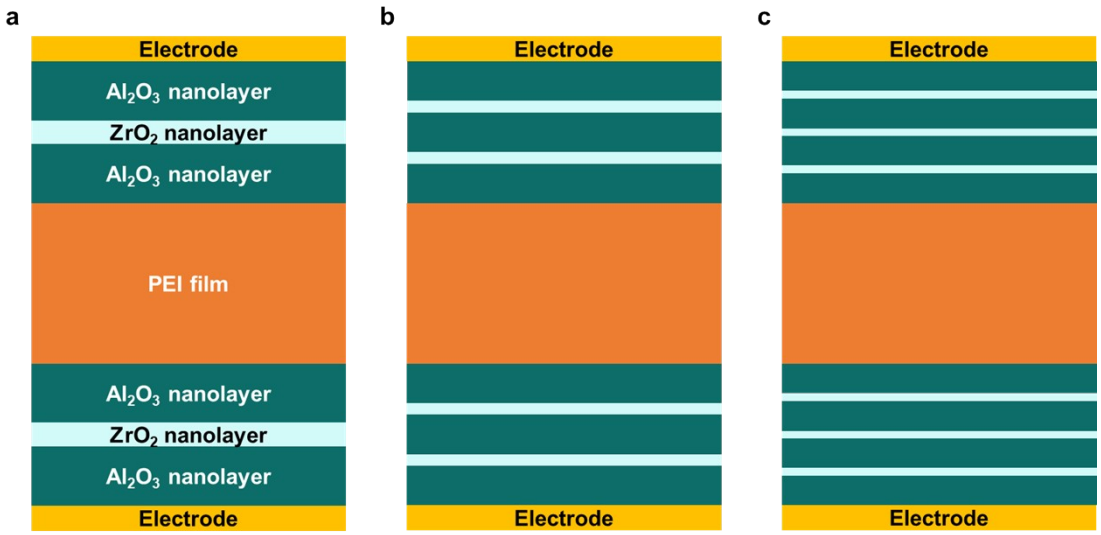

Figure S1. Schematic diagram of (a) 3-PEI, (a) 5-PEI, and (c) 7-PEI.

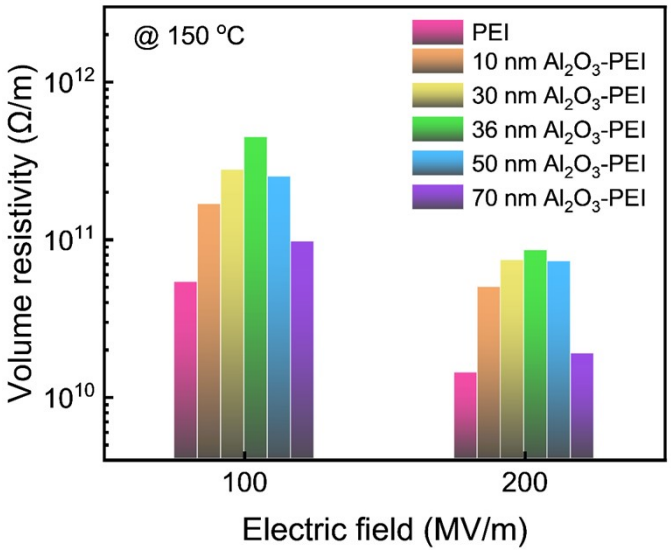

Figure S2. Volume resistivity of pristine PEI and Al_2O_3-coated PEI films with varying Al_2O_3 deposition thicknesses, measured at 150 °C.

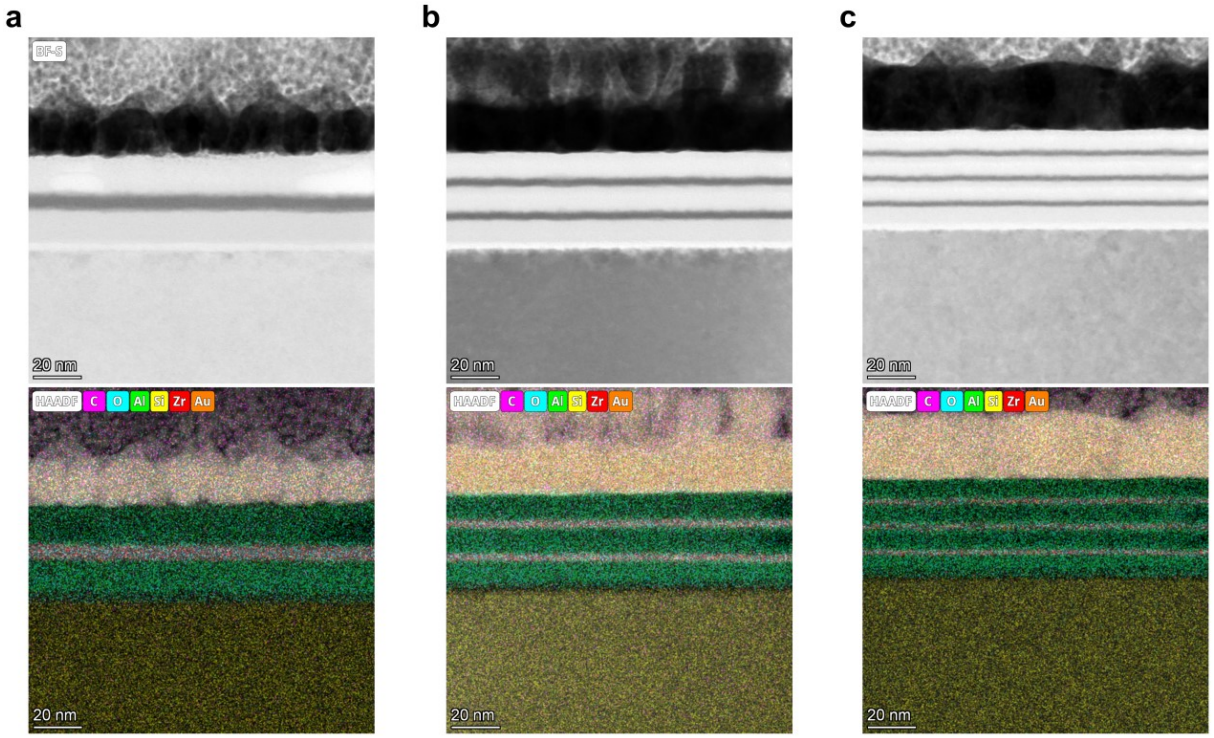

Figure S3. Cross-sectional TEM images and corresponding EDX mapping images of Al_2O_3/ZrO_2 alternating nanolaminates with (a) 3 layers, (b) 5 layers, and (c) 7 layers. The nanolaminates films were deposited on single-crystal silicon substrates for FIB-TEM characterization. To ensure structural integrity during FIB milling, a protective gold layer was sputter-coated onto the film surface before milling.

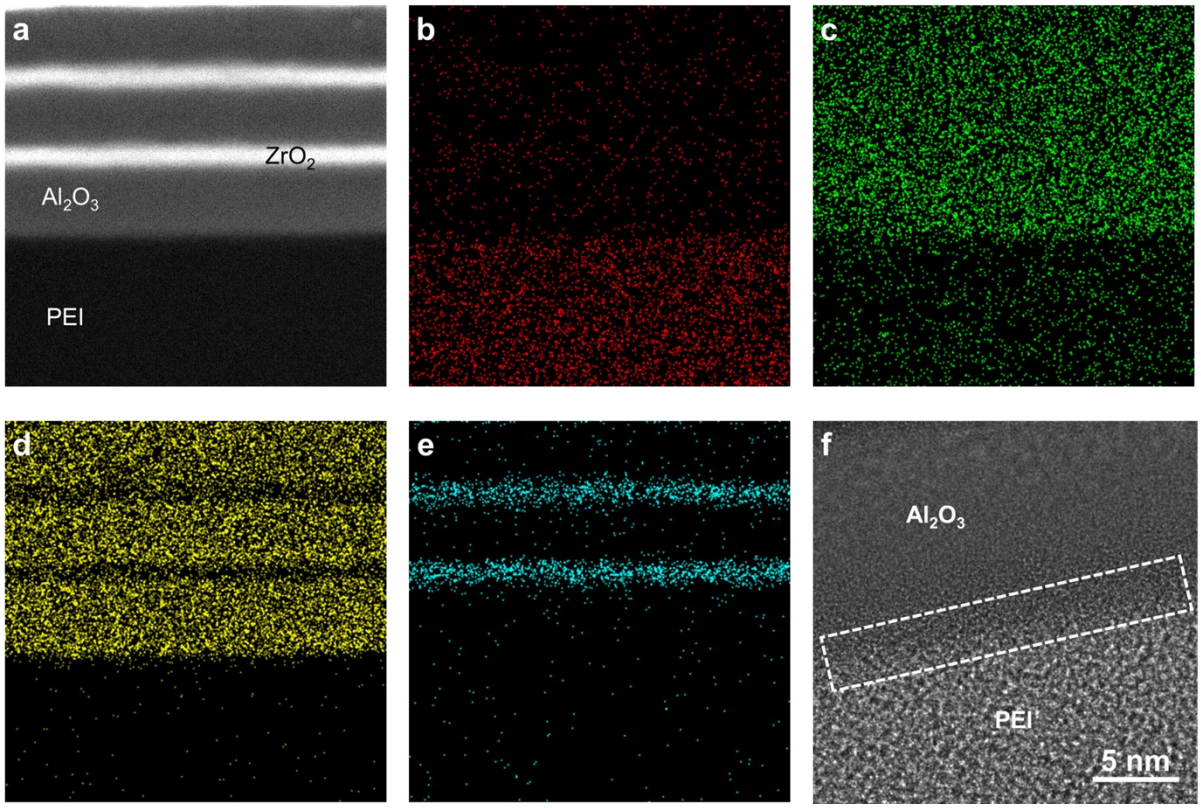

Figure S4. (a) Cross-sectional TEM image of the alternating Al_2O_3/ZrO_2 nanolaminate on a PEI film. Corresponding EDX elemental maps of (b) C, (c) O, (d) Al, and (e) Zr. (f) High-resolution TEM image showing the interface between the Al_2O_3/ZrO_2 nanolaminate and the PEI substrate.

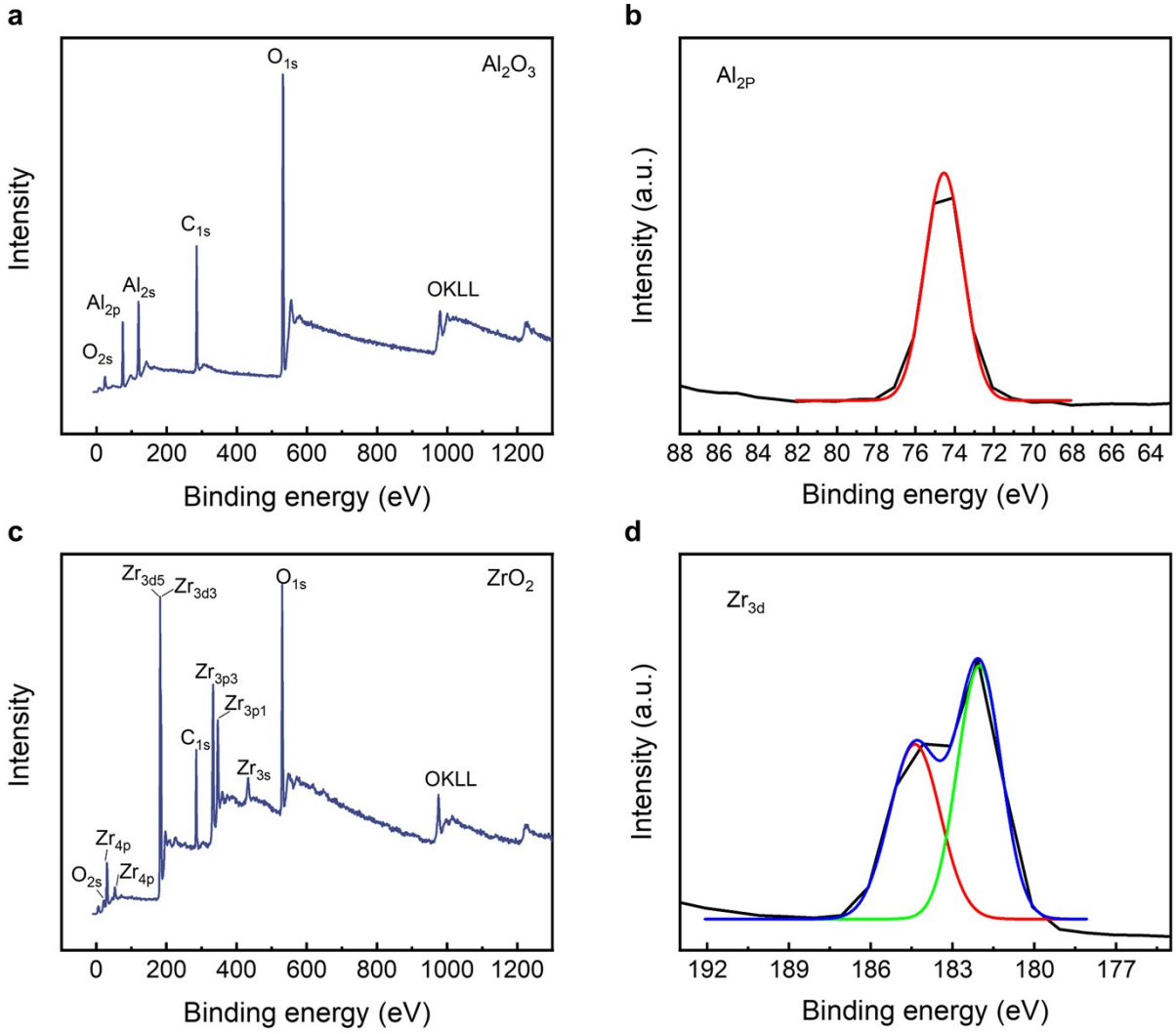

Figure S5. (a) XPS spectra of Al_2O_3 layer on Si substance, core level XPS spectra of (b) Al_{2p}. (d) XPS spectra of ZrO_2 layer on Si substance, core level XPS spectra of (e) Zr_{3d}.

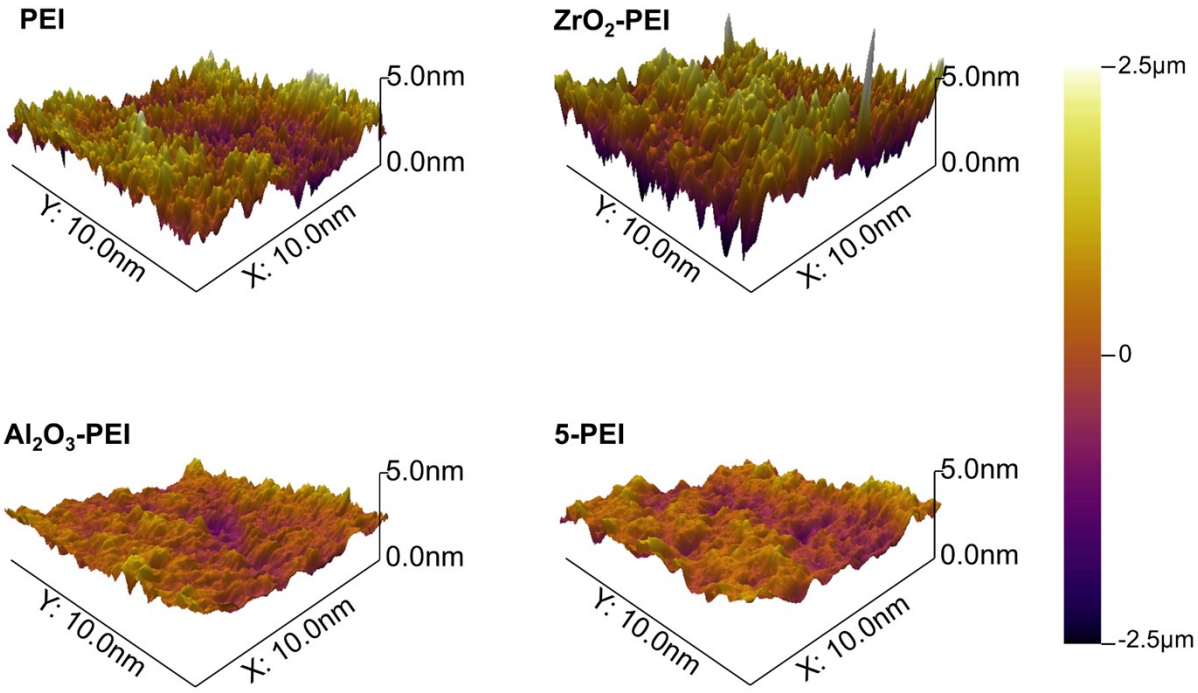

Figure S6. AFM images of pristine PEI, ZrO_2-PEI, Al_2O_3-PEI, and 5-PEI film.

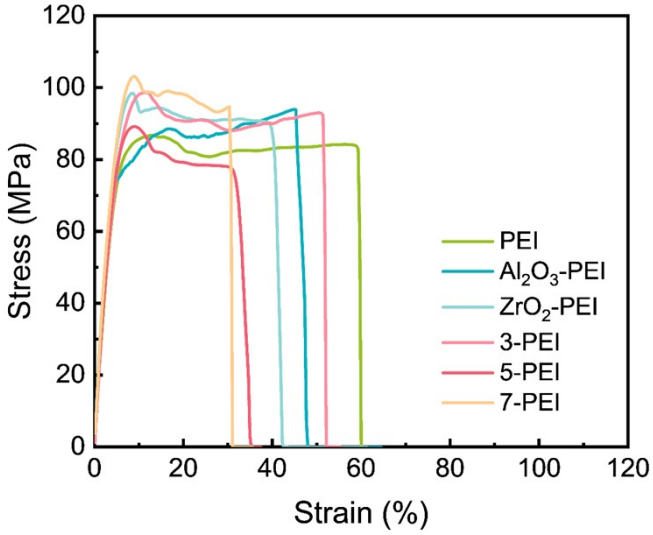

Figure S7. Stress-strain curves of pristine PEI and PEI-based films.

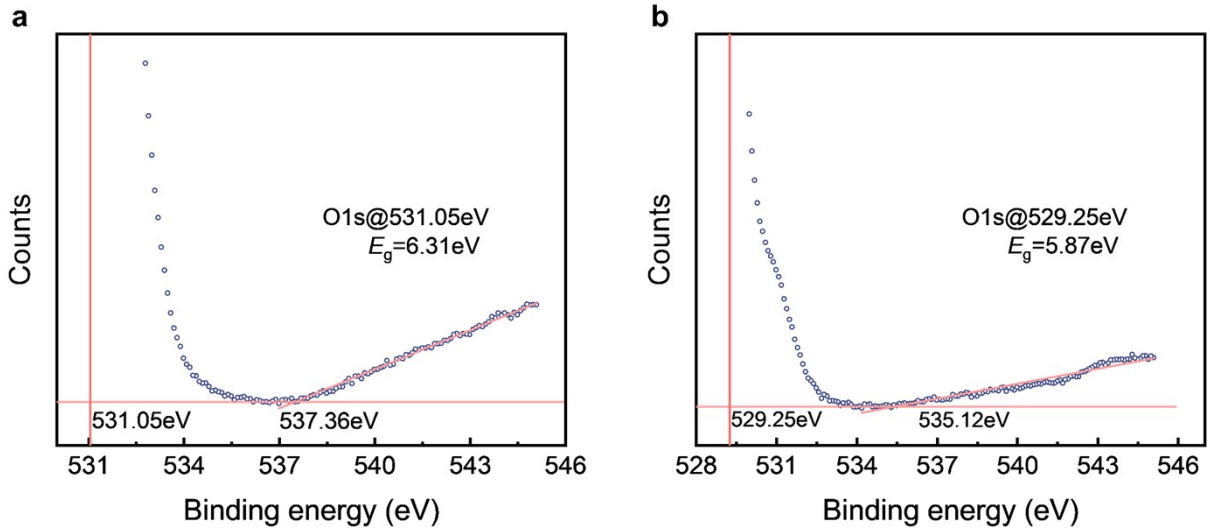

Figure S8. Bandgap values of Al_2O_3 and ZrO_2 coating layer derived from the onset of XPS O1s spectra.

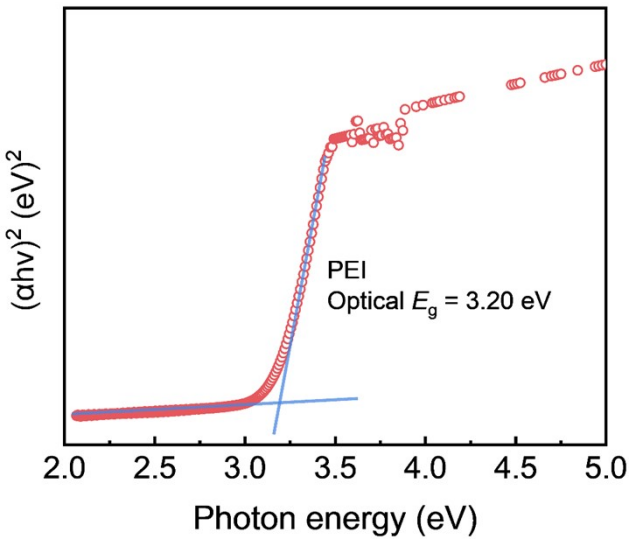

Figure S9. Measurement of the bandgap for PEI film from UV-Vis absorption spectroscopy.

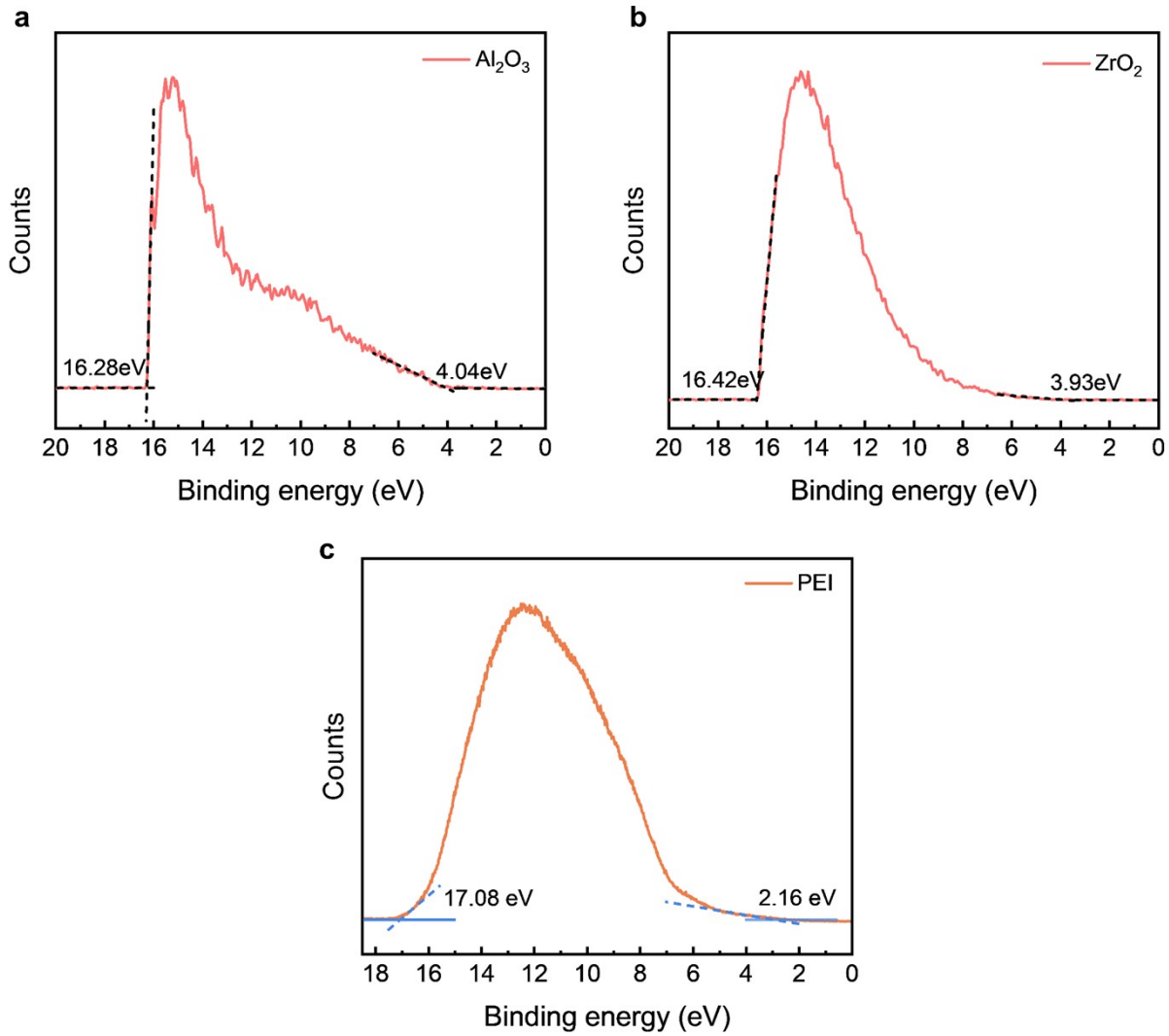

Figure S10. Ultraviolet photoelectron spectroscopy (UPS) spectrum of (a) Al_2O_3, (b) ZrO_2 coating layer, and (c) PEI film.

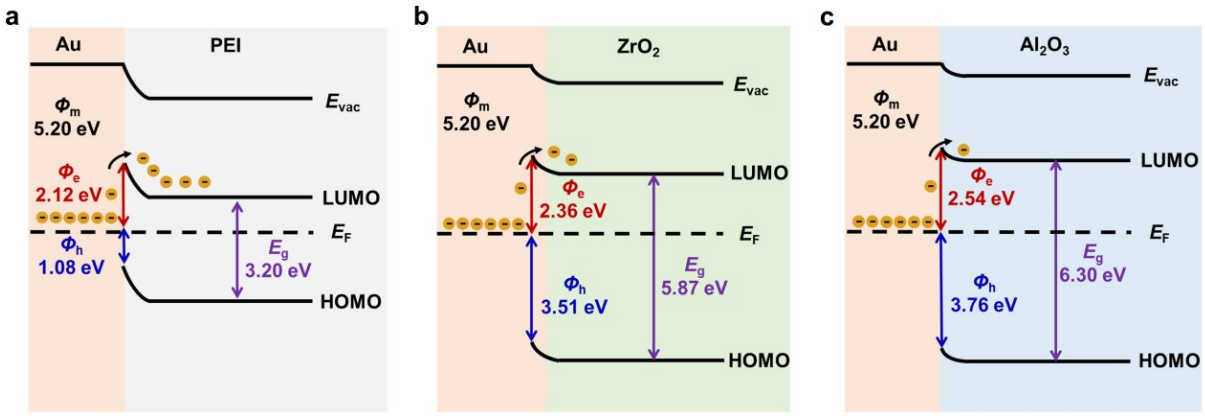

Figure S11. Band diagrams at the electrode/dielectric interface of (a) Au/PEI, (b) Au/ZrO_2, and (c) Au/Al_2O_3. E_{vac} is the vacuum energy level; E_F is the Fermi energy level. LUMO, HOMO, Φ_e, Φ_h is the lowest unoccupied molecular orbital, highest occupied molecular orbital, potential barrier for electrons, and potential barriers for holes, respectively.

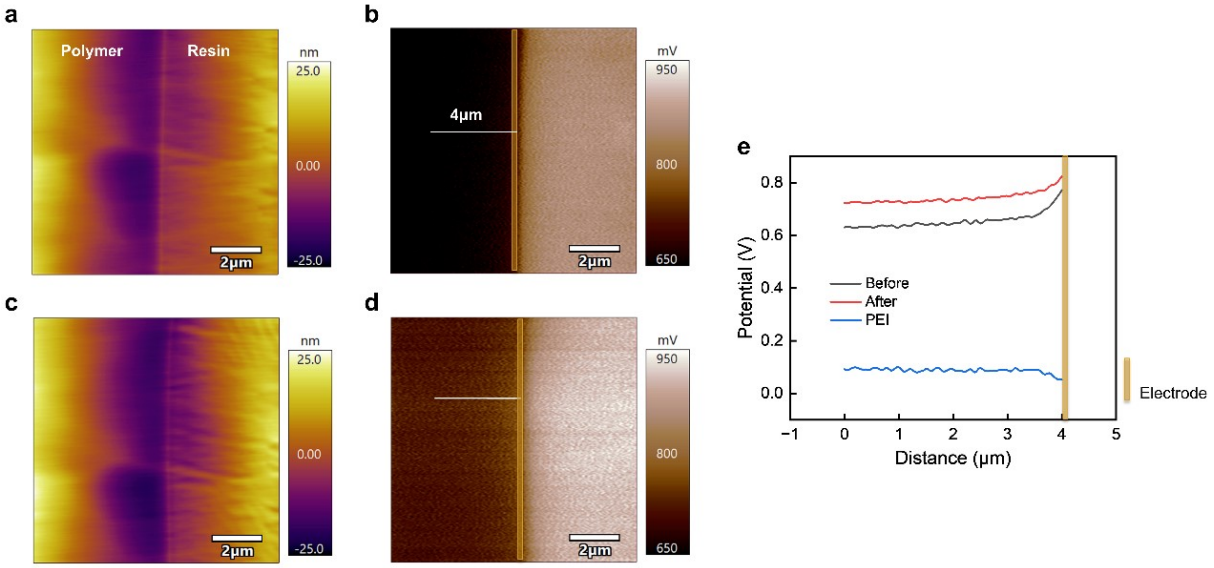

Figure S12. (a) Surface morphology and (b) surface potential distribution of the pristine PEI film in the initial state. (c) Surface morphology and (d) surface potential distribution of the pristine PEI film after the charging/discharging process. (e) Comparison of the surface potential at the marked position of the pristine PEI film measured by KPFM before and after charging.

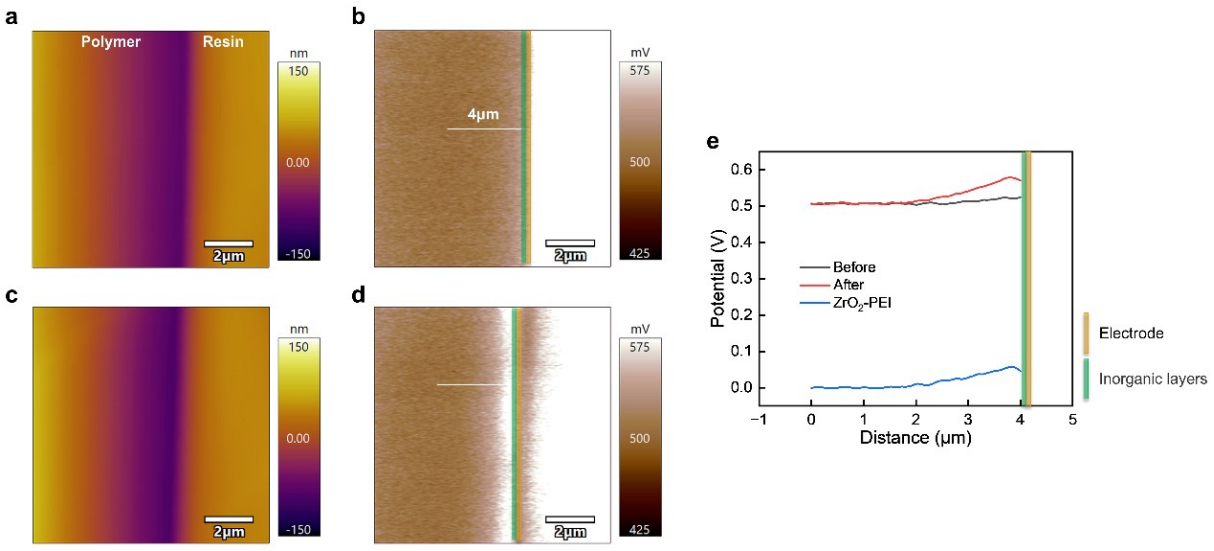

Figure S13. (a) Surface morphology and (b) surface potential distribution of the ZrO_2-PEI film in the initial state. (c) Surface morphology and (d) surface potential distribution of the ZrO_2-PEI film after the charging/discharging process. (e) Comparison of the surface potential at the marked position of the ZrO_2-PEI film measured by KPFM before and after charging.

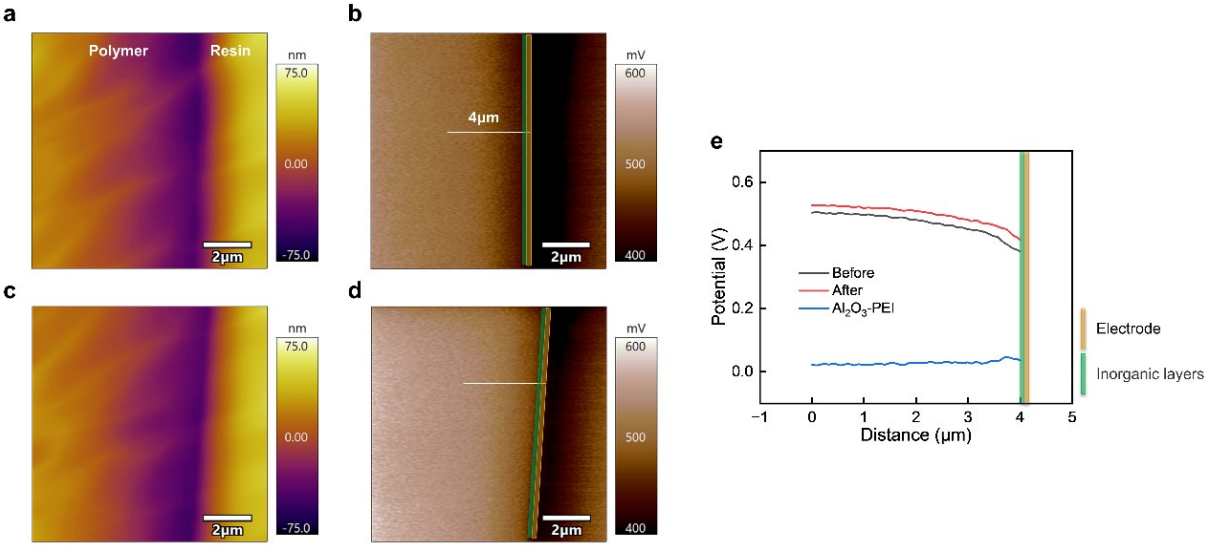

Figure S14. (a) Surface morphology and (b) surface potential distribution of the Al_2O_3-PEI film in the initial state. (c) Surface morphology and (d) surface potential distribution of the Al_2O_3-PEI film after the charging/discharging process. (e) Comparison of the surface potential at the marked position of the Al_2O_3-PEI film measured by KPFM before and after charging.

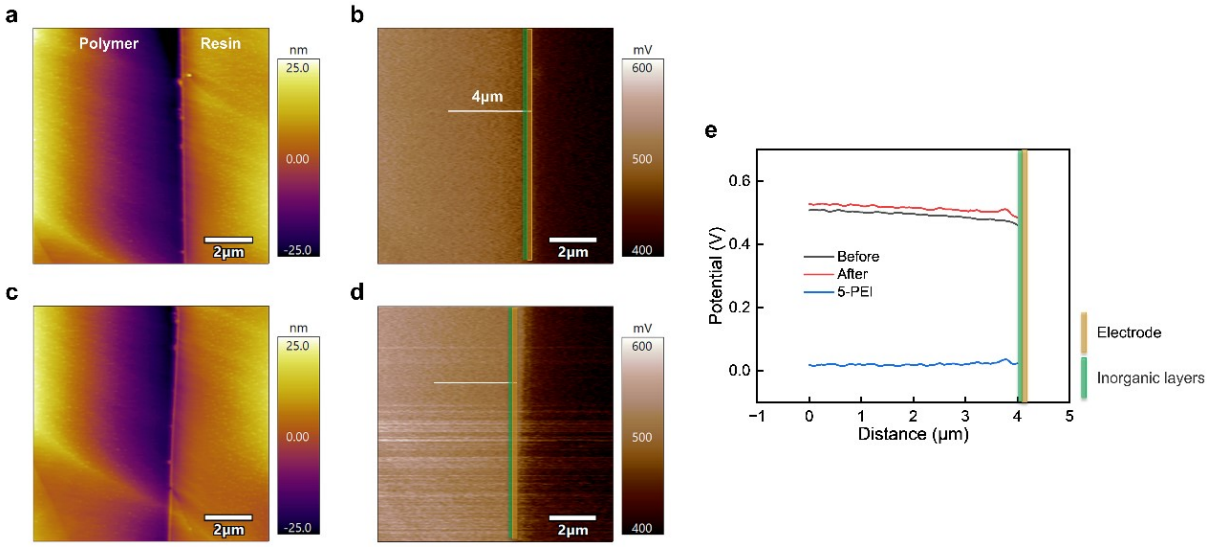

Figure S15. (a) Surface morphology and (b) surface potential distribution of the 5-PEI film in the initial state. (c) Surface morphology and (d) surface potential distribution of the 5-PEI film after the charging/discharging process. (e) Comparison of the surface potential at the marked position of the 5-PEI film measured by KPFM before and after charging.

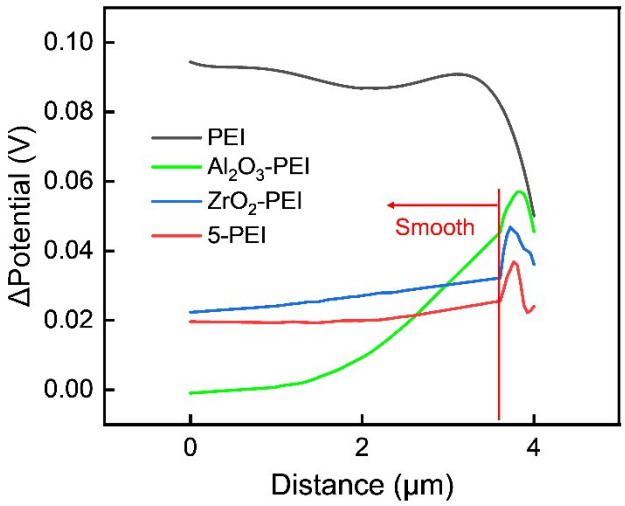

Figure S16. Smoothed surface potential difference between the initial state and the charged–discharged state of each sample, with the material–electrode interface located at 4 μm.

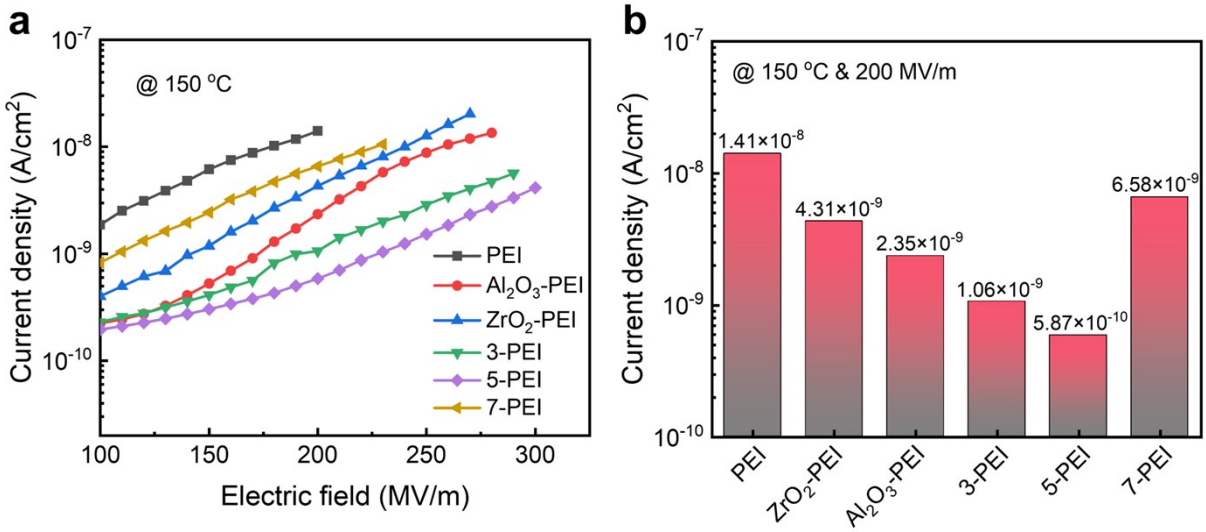

Figure S17. (a) Leakage current density as a function of electric field for pristine PEI and PEI-based films measured at 150 °C. (b) Leakage current density for pristine PEI and PEI-based films measured at 150 °C and 200 MV m^{-1}.

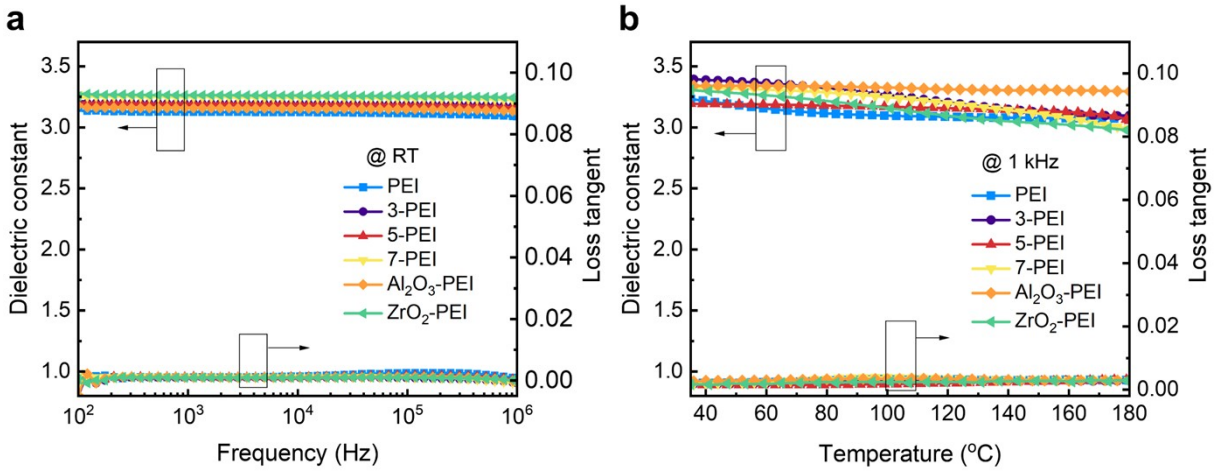

Figure S18. (a) Frequency-dependent and (b) temperature-dependent dielectric spectra of pristine PEI and PEI-based films measured at room temperature and 1 kHz, respectively.

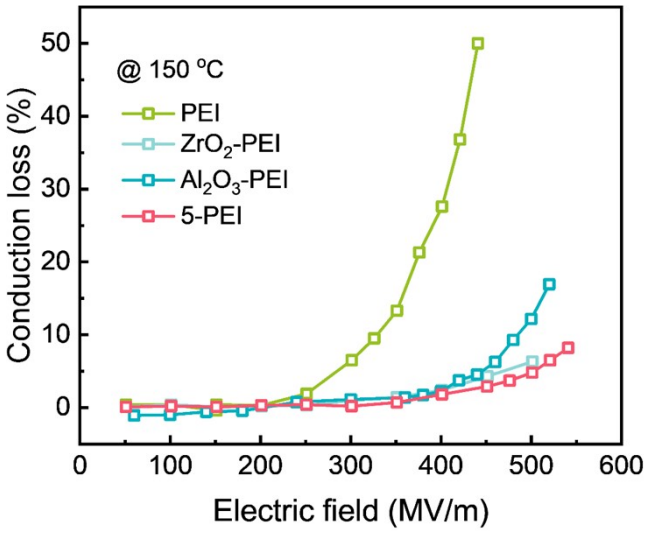

Figure S19. Conduction loss of pristine PEI, ZrO_2-PEI, Al_2O_3-PEI, and 5-PEI film at 150 °C as a function of the applied electric field.

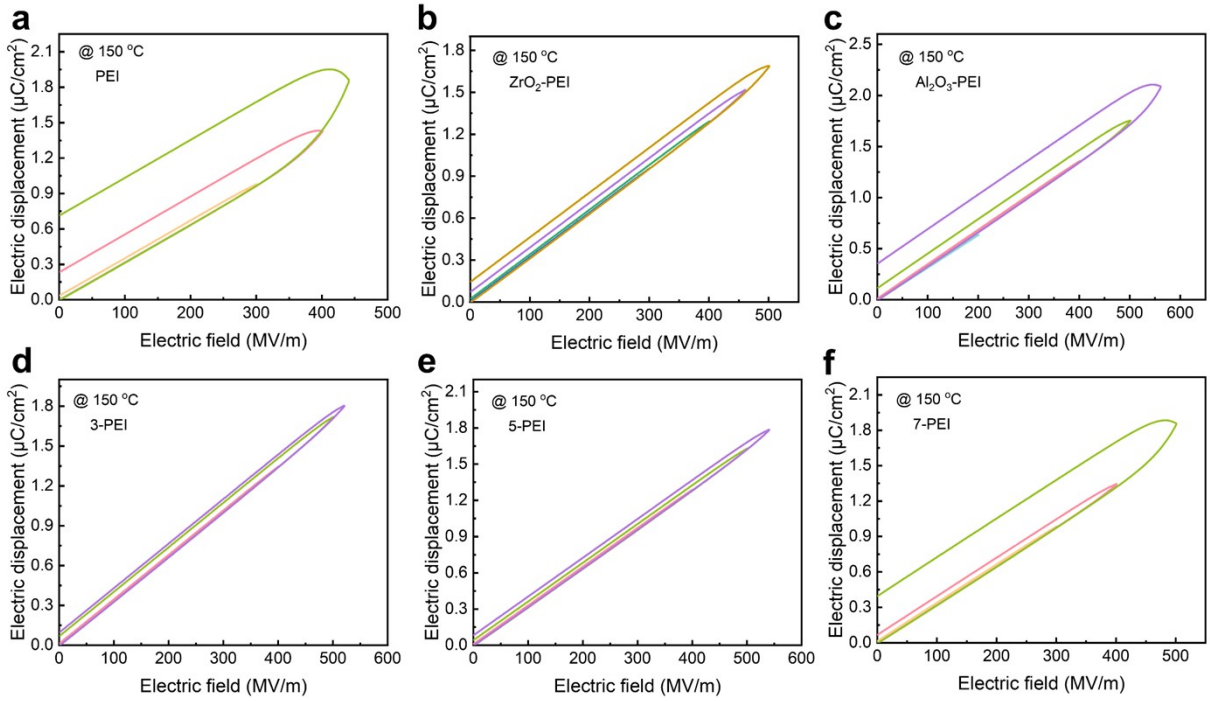

Figure S20. *D-E* loops of (a) pristine PEI, (b) ZrO_2-PEI, (c) Al_2O_3-PEI, (d) 3-PEI, (e) 5-PEI, and (f) 7-PEI films at 150 °C.

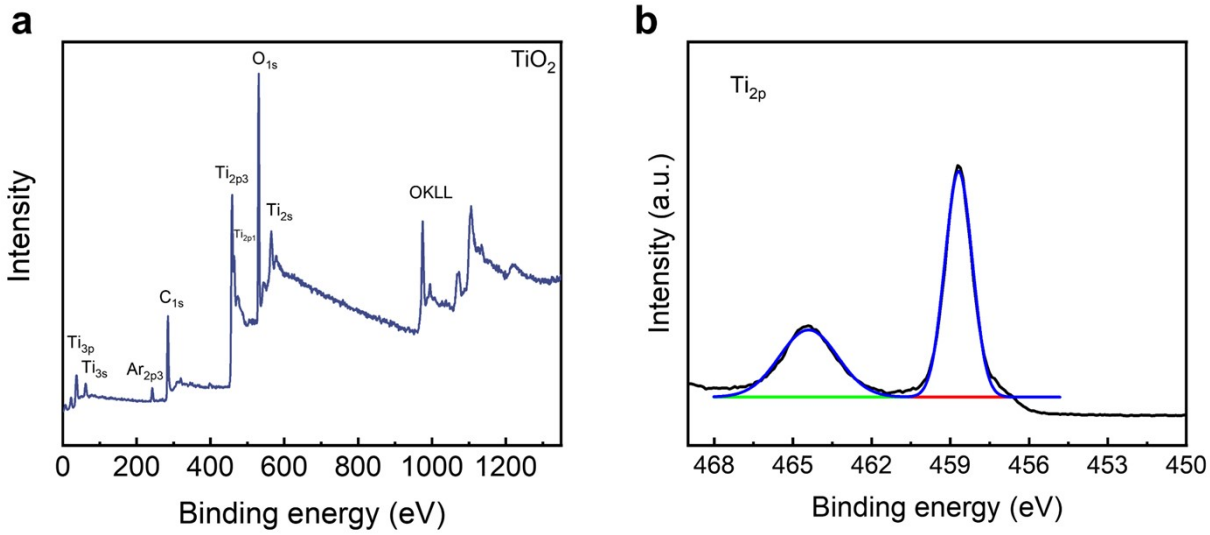

Figure S21. (a) XPS spectra of TiO_2 layer on Si substance, core level XPS spectra of (b) Ti_{2p}.

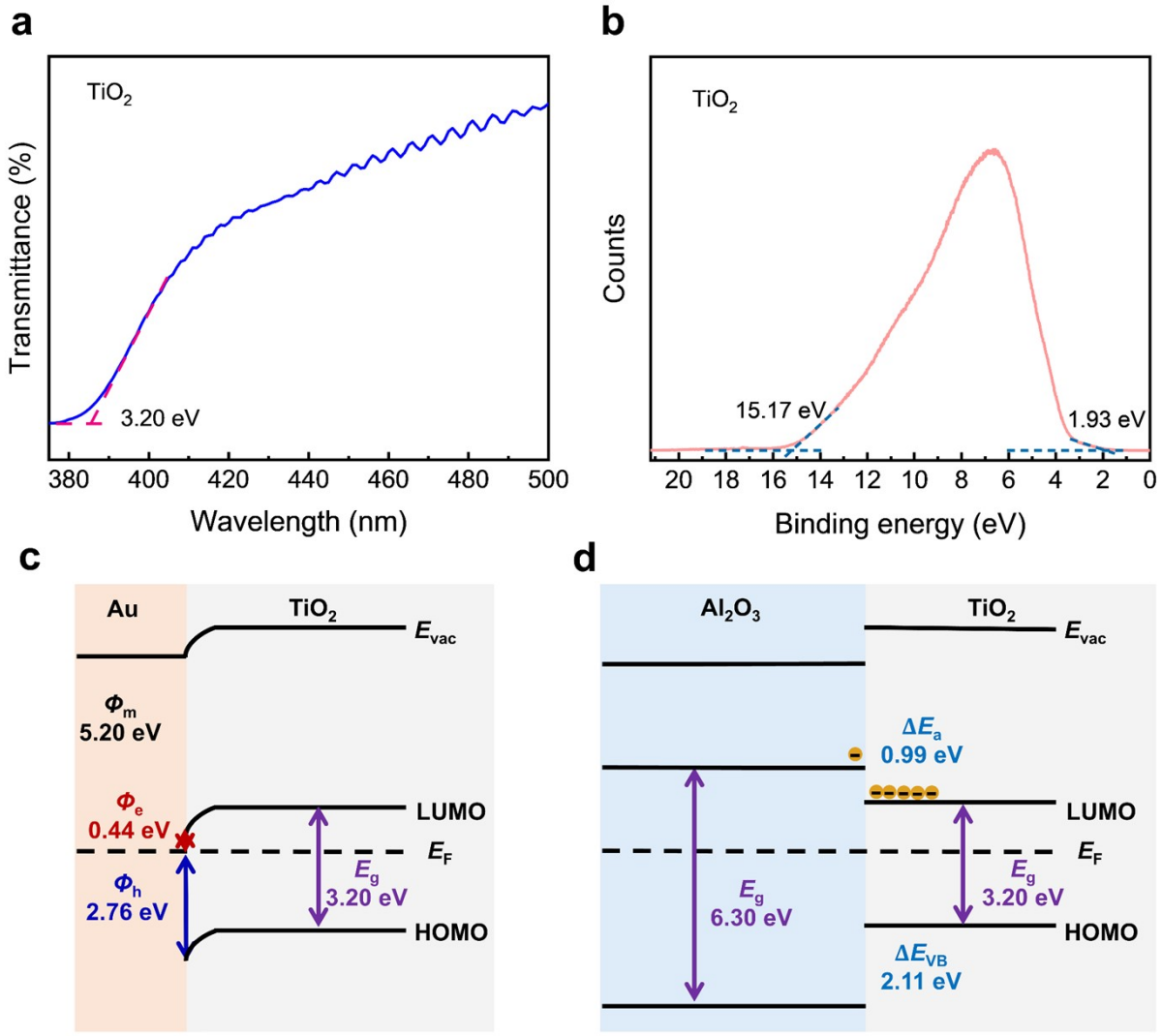

Figure S22. (a) Measurement of the bandgap for TiO_2 layer from UV-Vis absorption spectroscopy. (b) UPS spectrum of TiO_2 coating layer. Band diagrams at the electrode/dielectric interface of (c) Au/TiO_2 and (d) alternating Al_2O_3/TiO_2 nanolaminate.

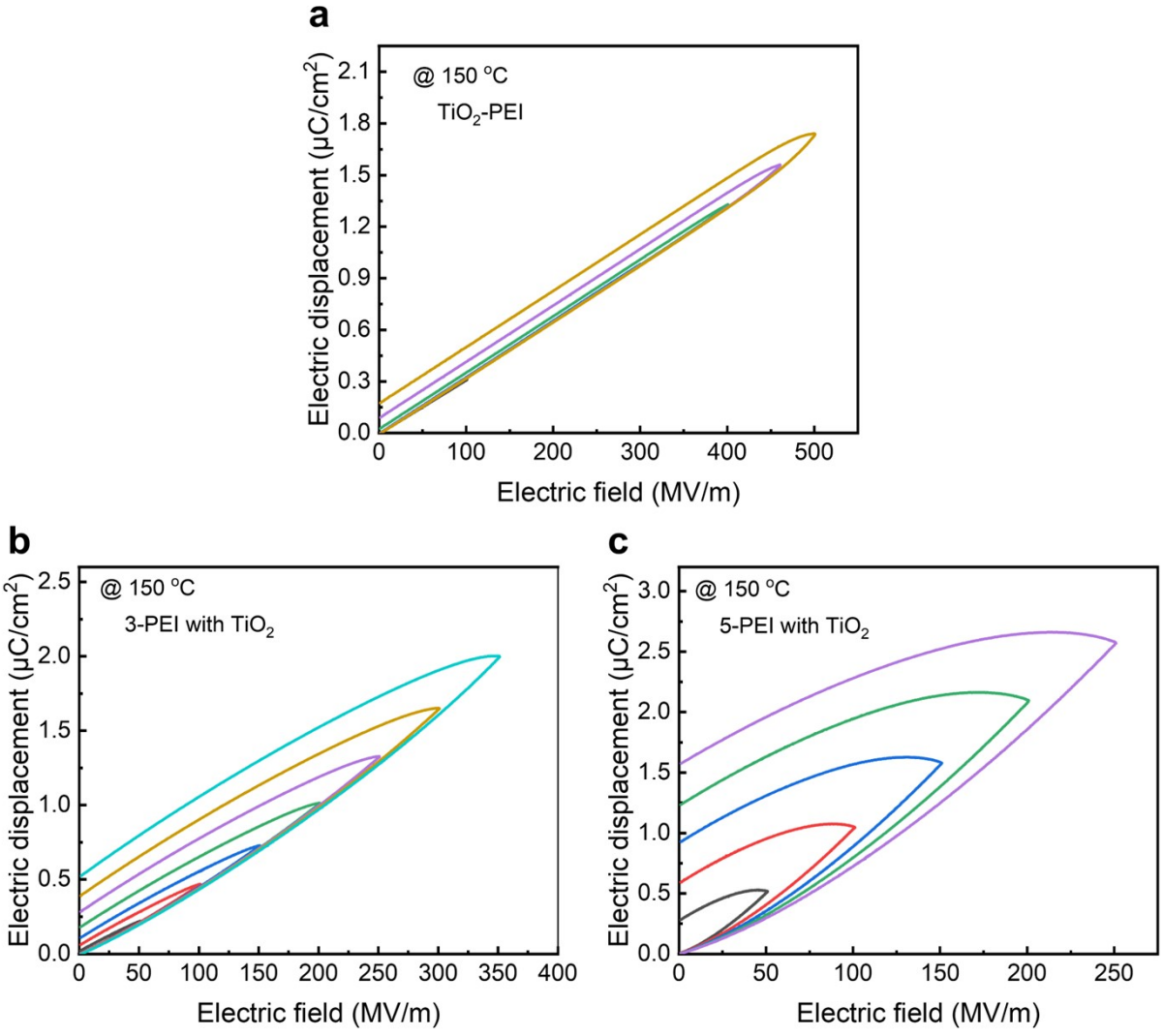

Figure S23. *D-E* loops of (a) TiO_2-PEI, (b) 3-PEI with TiO_2, and (c) 5-PEI with TiO_2 films at 150 °C.

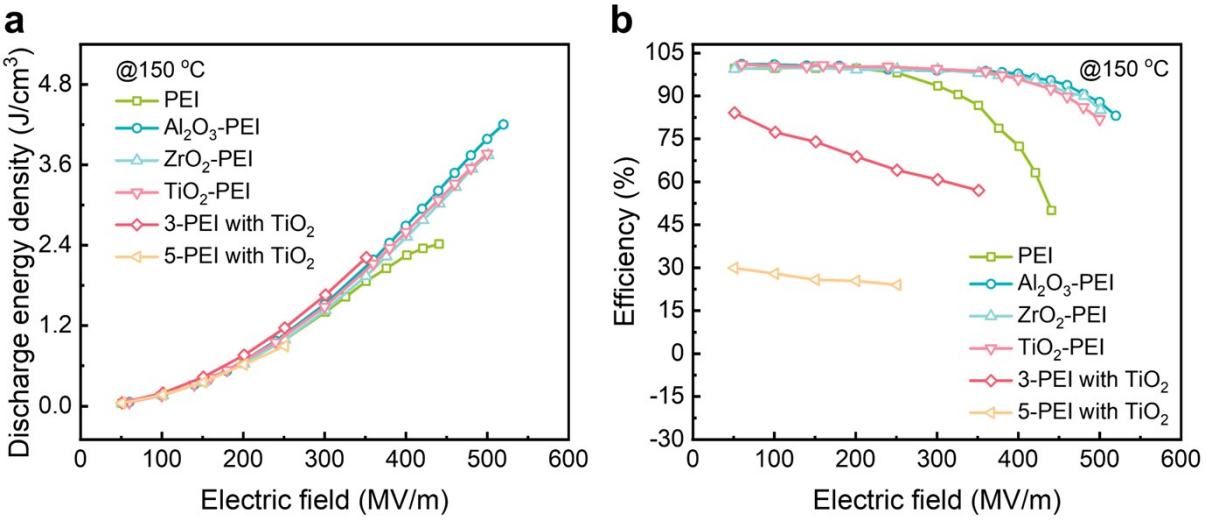

Figure S24. (a) Discharged energy density and (b) charge-discharge efficiency of PEI, Al_2O_3-PEI, ZrO_2-PEI, TiO_2-PEI, 3-PEI with TiO_2, and 5-PEI with TiO_2 films at 150 °C.

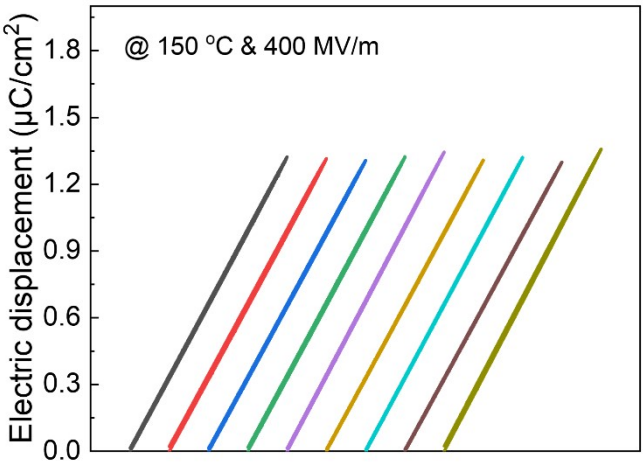

Figure S25. *D–E* loops of different regions in the 5-PEI film at 150 °C under 400 MV m^{-1}.

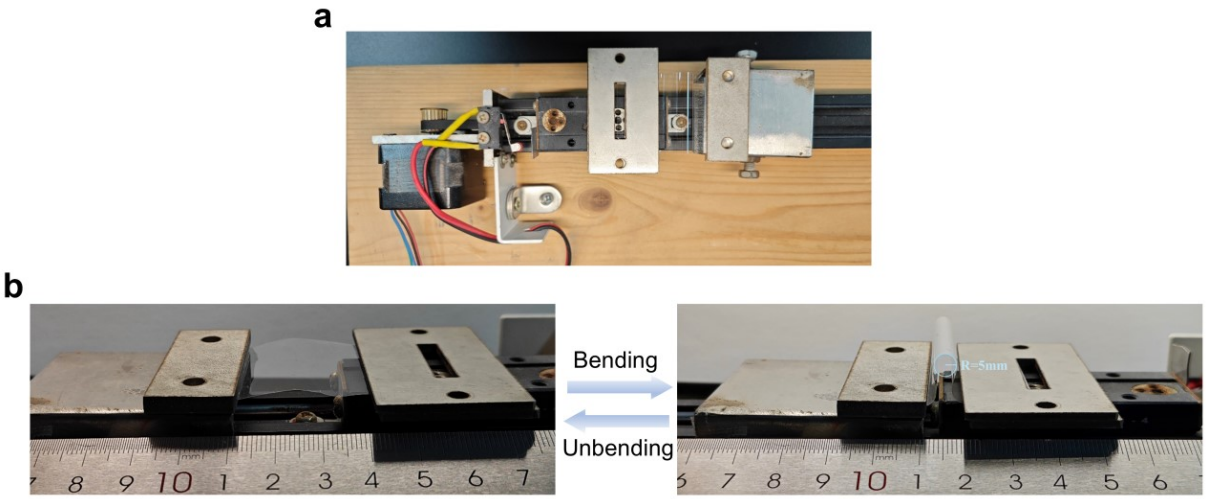

Figure S26. (a) Digital photographs of experimental setup of the bending test. (b) The 5-PEI films strip repeatedly for a straight 10,000 rounds, and each round is programmed to be accomplished in 5 seconds. Since film capacitors are typically wound into cylindrical rolls, the polymer films must exhibit adequate resistance to flexural fatigue. Figure S20 shows the laboratory-built mechanical fatigue testing apparatus for polymer films, which consists of a test control module, a stepper motor, and sample motion rails. The number of bending cycles and the travel distance of the sample are controlled *via* dedicated computer software.

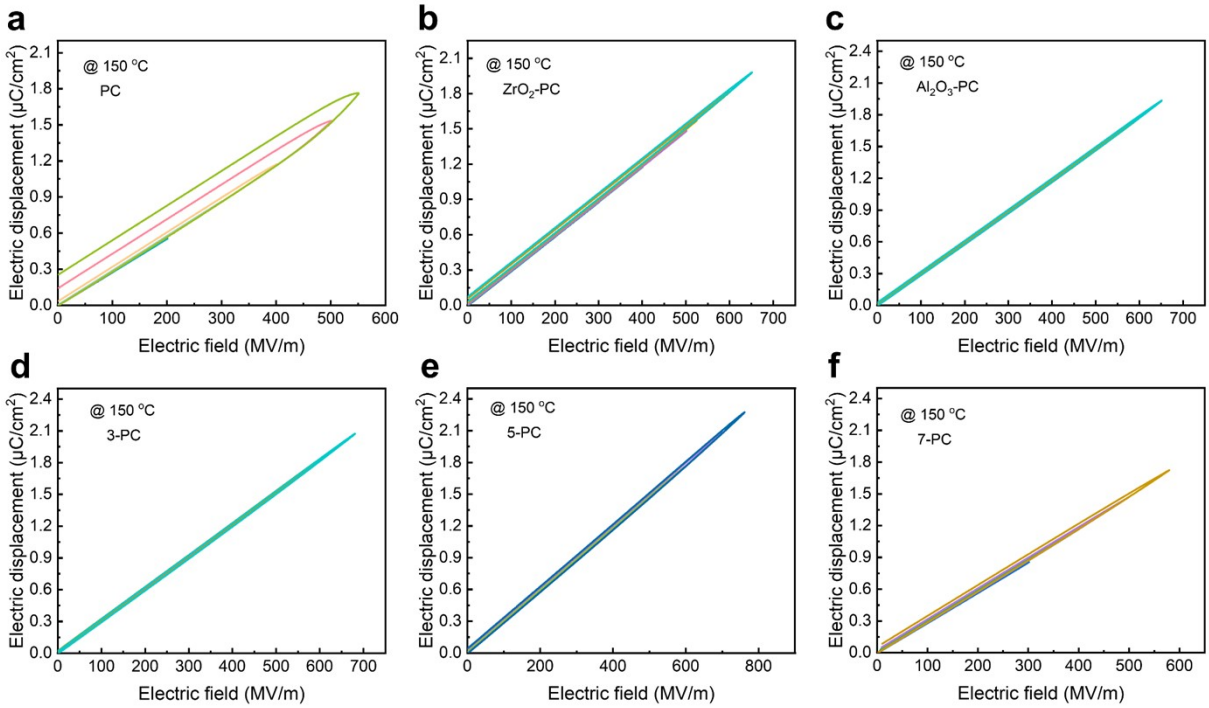

Figure S27. *D-E* loops of (a) pristine PC, (b) ZrO_2-PC, (c) Al_2O_3-PC, (d) 3-PC, (e) 5-PC, and (f) 7-PC films at 150 °C.

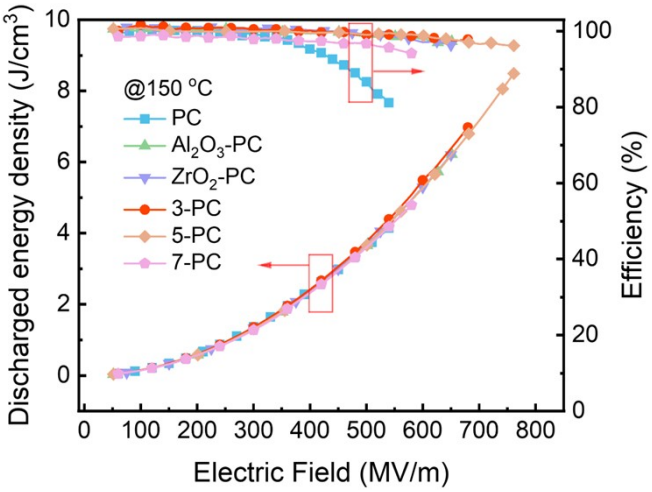

Figure S28. Energy storage performance of PC and PC-based films at 150 °C.

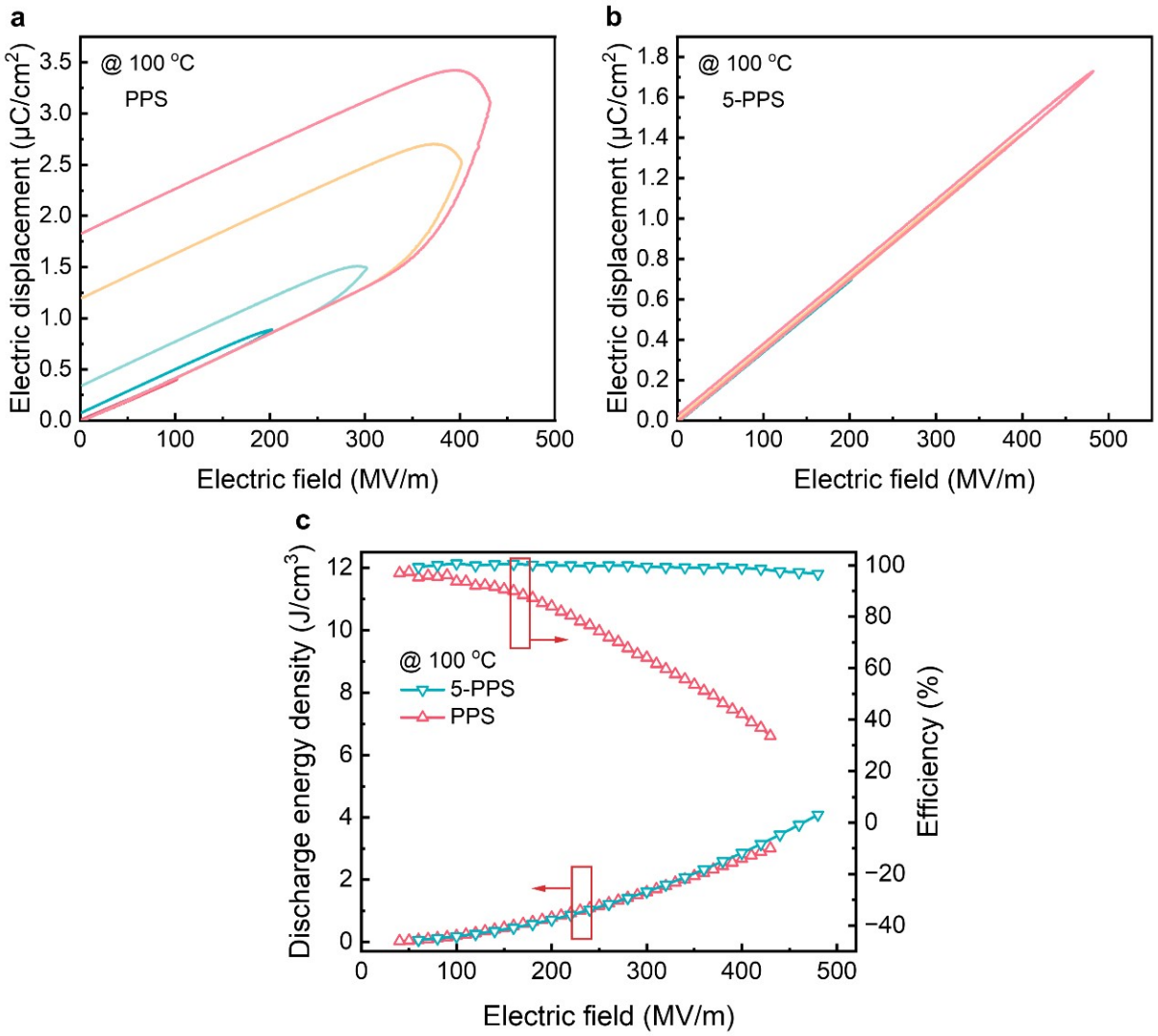

Figure S29. (a) *D-E* loops of pristine PPS at 100 °C. (b) *D-E* loops of 5-PPS at 100 °C. (c) Energy storage properties of pristine PPS and 5-PPS at 100 °C.

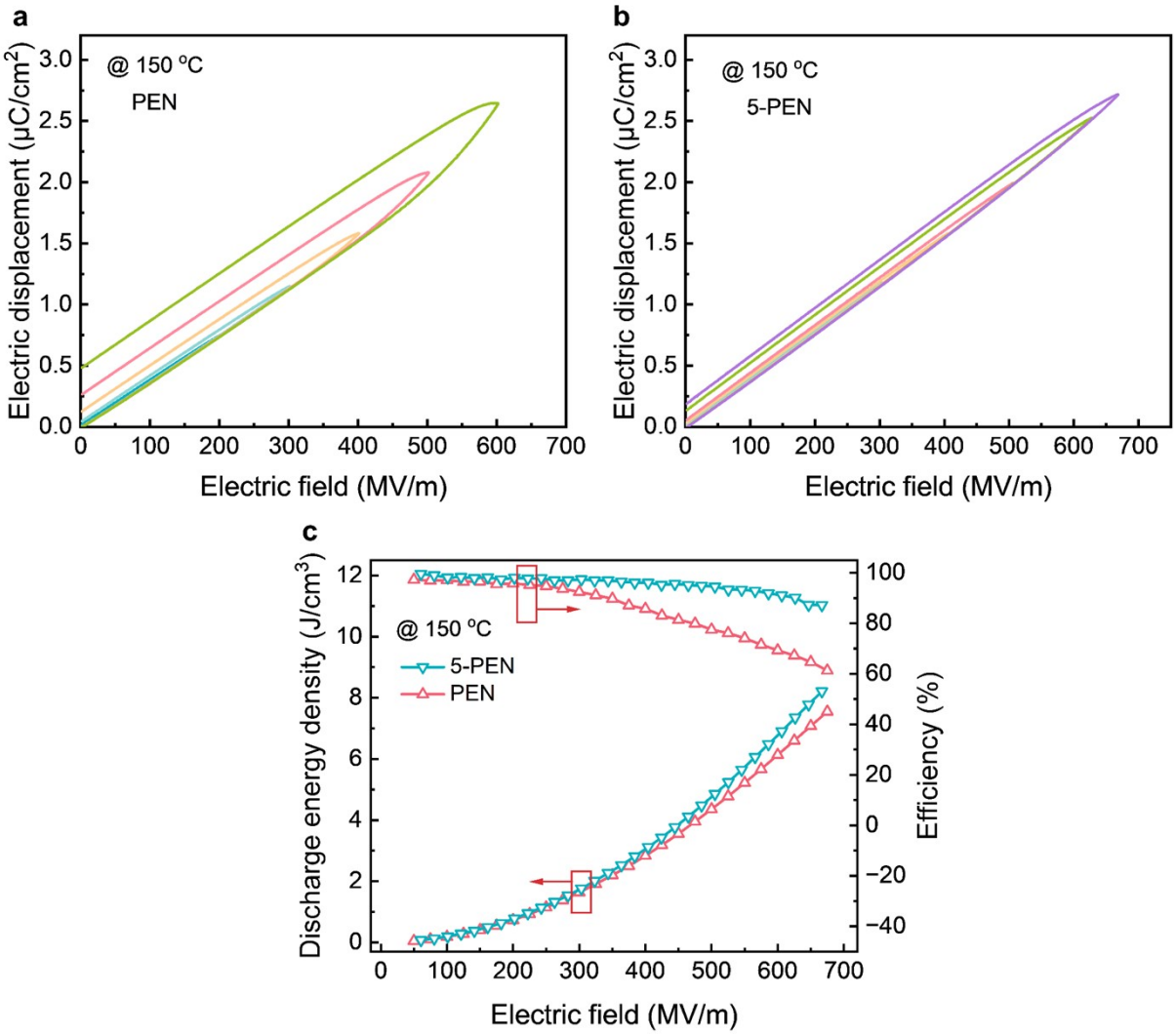

Figure S30. (a) *D-E* loops of pristine PEN at 150 °C. (b) *D-E* loops of 5-PEN at 150 °C. (c) Energy storage properties of pristine PEN and 5-PEN at 150 °C.

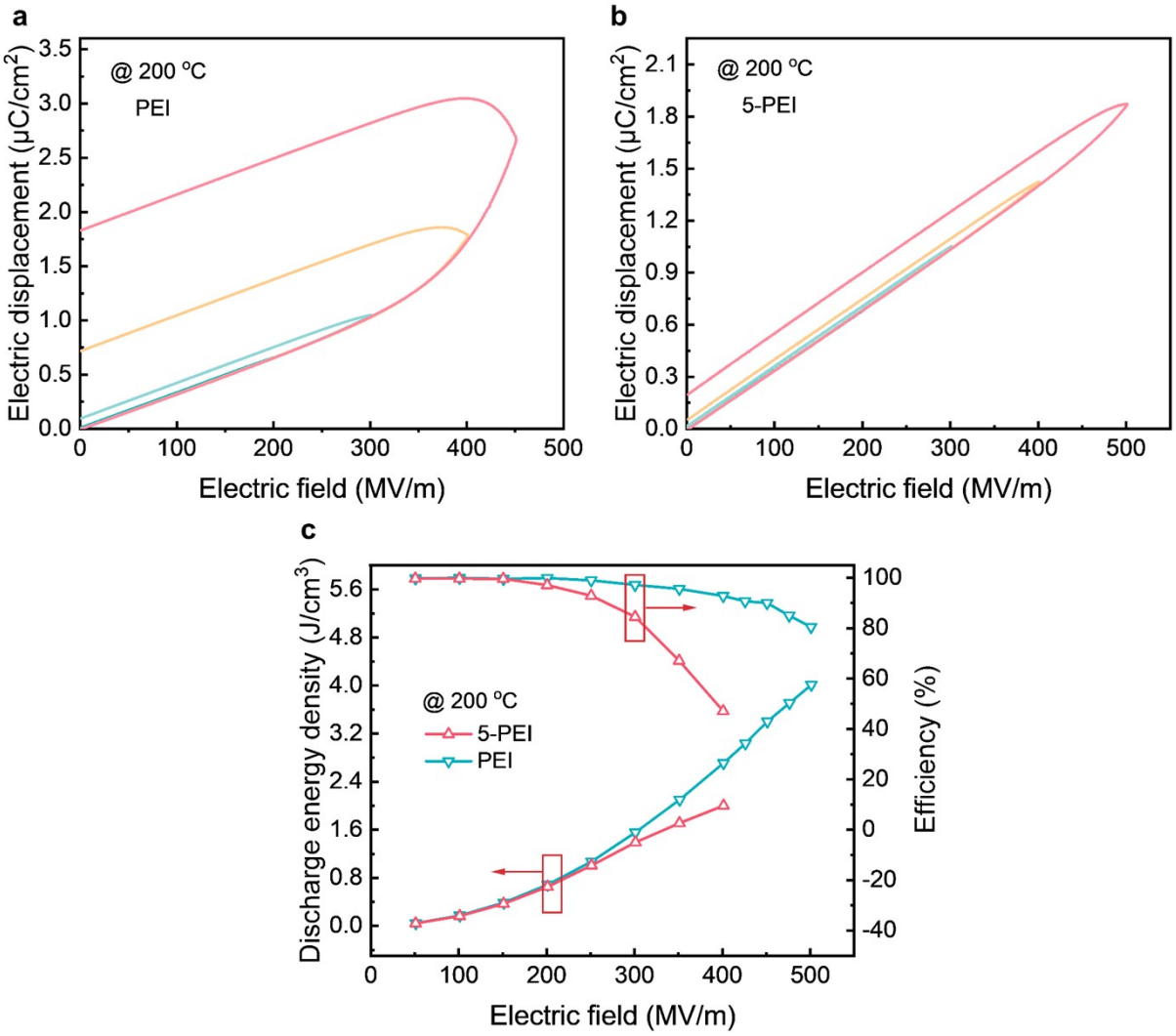

Figure S31. (a) *D-E* loops of pristine PEI at 200 °C. (b) *D-E* loops of 5-PEI at 200 °C. (c) Energy storage properties of pristine PEI and 5-PEI at 200 °C.

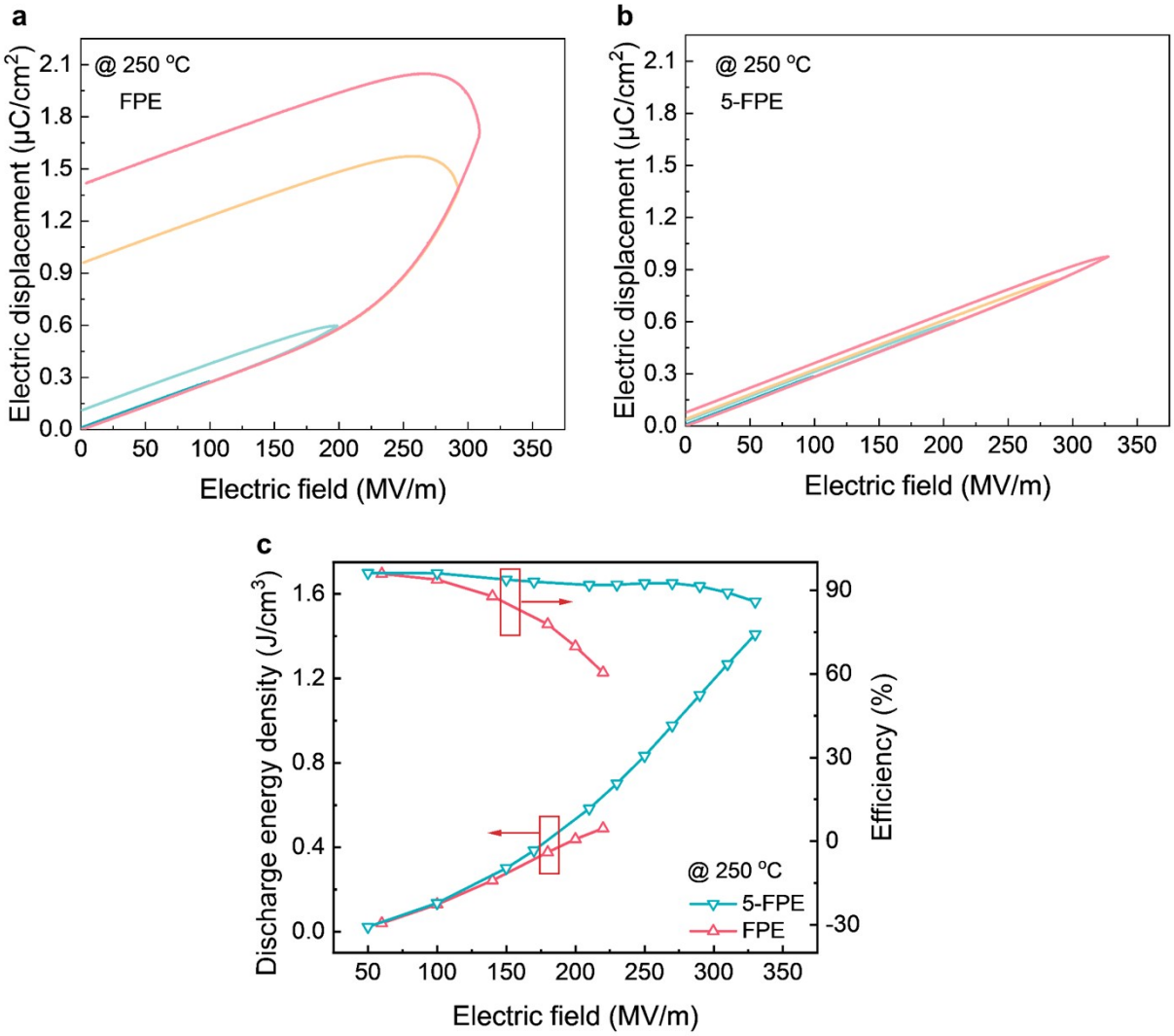

Figure S32. (a) *D-E* loops of pristine FPE at 250 °C. (b) *D-E* loops of 5-FPE at 250 °C. (c) Energy storage properties of pristine FPE and 5-FPE at 250 °C.

Table S1. ALD deposition sequences for the oxide films, with times corresponding to the durations required for a single ALD cycle.

Oxide	Precursor	Pulse Time (s)	N_2 Purge Time (s)	Water Vapor Pulse Time (s)	N_2 Purge Time (s)
Al_2O_3	TMA	2	30	0.5	30
ZrO_2	TDMZ	0.3	30	0.3	40
TiO_2	TDMAT	0.3	40	0.3	60

Table S2. Material parameters at 150 ℃ used in the phase-field simulation.[S4,S5]

Materials	Dielectric constant	Electric conductivity (S m^{-1})	Breakdown strength (MV m^{-1})
PEI	3.2	1×10^{-10}	400
ZrO_2	20	1×10^{-13}	600
Al_2O_3	9	4×10^{-13}	1000

Table S3. The surface roughness of pristine PEI, ZrO_2-PEI, Al_2O_3-PEI, and 5-PEI film.

Samples	Root mean square roughness [Rq] (pm)	Arithmetic average roughness [Ra] (pm)
PEI	788.057	634.303
ZrO_2-PEI	760.733	594.279
Al_2O_3-PEI	391.696	304.510
5-PEI	424.330	343.304

References

S1. L. A. Dissado, J. C. Fothergill, S. V. Wolfe, and R. M. Hill, *IEEE Trans. Electr. Insul.*, 1984, **19**, 227–233.

S2. B. Zhang, W. Guo, Y. H. Sun, W. H. Han, and G. J. Zhang, *Phys. Plasmas*, 2024, **31**, 053503.

S3. K. X. Li, B. Y. Zhang, Z. Y. Yang, M. H. Yao, Y. X. Li, J. Li, Z. Zintak, Q. R. Yuchi, and X. W. Li, *ACS Appl. Mater. Interfaces*, 2025, **17**, 25894–25902.

S4. S. Cheng, Y. Zhou, Y. S. Li, C. Yuan, M. C. Yang, J. Fu, J. Hu, J. L. He, and Q. Li, *Energy Storage Mater.*, 2021, **42**, 445–453.

S5. J. F. Dong, R. C. Hu, X. W. Xu, J. Chen, Y. J. Niu, F. Wang, J. Y. Hao, K. Wu, Q. Wang, and H. Wang, *Adv. Funct. Mater.*, 2021, **31**, 2102644.